Science Bulletin 64 (2019) 976–985

Contents lists available at ScienceDirect

Science Bulletin

journal homepage: www.elsevier.com/locate/scib

Article

Encapsulating a Ni(II) molecular catalyst in photoactive metal–organic framework for highly efficient photoreduction of CO_2

Zhi-Hao Yan [a], Bo Ma [a], Shu-Rong Li [a], Junxue Liu [b], Rong Chen [a], Ming-Hao Du [a], Shengye Jin [b,*], Gui-Lin Zhuang [c], La-Sheng Long [a], Xiang-Jian Kong [a,*], Lan-Sun Zheng [a]

[a] Collaborative Innovation Center of Chemistry for Energy Materials, State Key Laboratory of Physical Chemistry of Solid Surface and Department of Chemistry, College of Chemistry and Chemical Engineering, Xiamen University, Xiamen 361005, China
[b] State Key Laboratory of Molecular Reaction Dynamics and Collaborative Innovation Center of Chemistry for Energy Materials, Dalian Institute of Chemical Physics, Chinese Academy of Sciences, Dalian 116023, China
[c] College of Chemical Engineering, Zhejiang University of Technology, Hangzhou 310032, China

ARTICLE INFO

Article history:
Received 26 February 2019
Received in revised form 20 April 2019
Accepted 16 May 2019
Available online 18 May 2019

Keywords:
Metal-organic frameworks
CO_2 reduction
Transient absorption
Photocatalysis
DFT calculations

ABSTRACT

Photocatalytic reduction of CO_2 to CO is a promising strategy for reducing atmospheric CO_2 levels and storing solar radiation as chemical energy. Here, we demonstrate that a molecular catalyst [Ni^{II}(bpet)$(H_2O)_2$] successfully encapsulated into a highly robust and visible-light responsive metal–organic framework (Ru-UiO-67) to fabricate composite catalysts for photocatalytic CO_2 reduction. The composite Ni@Ru-UiO-67 photocatalysts show efficient visible-light-driven CO_2 reduction to CO with a TON of 581 and a selectivity of 99% after 20-h illumination, because of the facile electron transfer from Ru-photosensitizer to Ni(II) active sites in Ni@Ru-UiO-67 system. The mechanistic insights into photoreduction of CO_2 have been studied based on thermodynamical, electrochemical, and spectroscopic investigation, together with density functional theory (DFT) calculations. This work shows that encapsulating molecular catalyst into photoactive MOF highlights opportunities for designing efficient, stable and recyclable photocatalysts.

1. Introduction

Carbon dioxide (CO_2) is regarded as a main source of the greenhouse effect, but it is also a chemical feedstock for carbon neutral sustainable energy [1]. The conversion of atmospheric CO_2 into industrially favorable chemicals/fuels such as CO, CH_4, CH_3OH, HCOOH and C_2H_6 is highly desired for the sake of environmental sustainability and renewable energy storage [2–4]. Therefore, artificial photosynthesis has attracted wide attentions with specific importance attached to the development of solar-light-driven reduction CO_2 into high value-added industrial chemicals [5–9]. A variety of inorganic semiconductor catalysts have been reported for photochemical conversion of CO_2 to carbon-based products [10–13]. However, these inorganic semiconductors have low densities of active sites on surfaces, limited tailorability, a large band gap, and the inevitable electron-hole recombination, causing the limited photocatalytic efficiencies. On the other hand, homogeneous molecular catalysts such as Fe [14,15], Co [16,17], Ni [18,19], and Mn [20,21] complexes usually exhibit good photocatalytic performances in reduction of CO_2, but the instability and recycling issues of homogeneous catalysis restrict their practical applications in photocatalysis [22]. Hence, the design and development of efficient, stable and recyclable photocatalysts are highly desirable.

Metal–organic frameworks (MOFs) are functional hybrid crystalline materials featuring well-defined porosity, high surface areas, and tunable structures. The unique features suggest that MOF materials are a class of ideal host matrices for immobilization of molecular catalysts, because that the composite materials not only display unique and synergistic functionalities but also can be easily recovered and reused for the long-term usage [23,24]. Recently, the controllable encapsulation of molecular catalysts into MOFs to form composite materials for photocatalytic hydrogen evolution reaction have made notable progress [25–28]. However, encapsulating the molecular catalysts into MOFs to enhance the catalytic activity in CO_2 reduction system has not been recognized yet. Among different molecular catalysts for photoreduction of CO_2, the nickel complexes have been demonstrated as one of the most promising candidate. A prominent advantage is that CO_2 could favorably bind to the nickel center and be activated, thus benefiting its conversion under solar irradiation [18]. Although

* Corresponding authors.
E-mail addresses: sjin@dicp.ac.cn (S. Jin), xjkong@xmu.edu.cn (X.-J. Kong).

https://doi.org/10.1016/j.scib.2019.05.014
2095-9273/

the catalytic activity of Ni(II) complex is high, the stability and recycling for catalyst are a significant challenge. To overcome the drawbacks, encapsulating the Ni(II) molecular catalysts into a stable and photosensitizing MOF will be a promising strategy to enhance the catalytic activity and reusability of the photocatalysts in CO_2 reduction system.

In this work, we selected a Ni(II) complex $[Ni^{II}(bpet)(H_2O)_2]\cdot(ClO_4)_2$ (bpet = 1,2-bis((pyridin-2-ylmethyl)thio)ethane) because of the high catalytic activity, and then design a composite molecular catalyst@MOF photocatalytic system $[Ni^{II}(bpet)(H_2O)_2]$@Ru-UiO-67 (simply as Ni@Ru-UiO-67) by encapsulating $[Ni^{II}(bpet)(H_2O)_2]$ into the cages of a visible-light photoactive MOF (Ru-UiO-67) through a "ship-in-a-bottle" approach. The photoreduction of CO_2 shows that the present Ni@Ru-UiO-67 not only possesses exceptional catalytic selectivity and activities but also exhibits high stability and good recyclability. The electron transfer (ET) dynamics of facile electron transfers from Ru-photocenters to Ni(II) catalytic centers were demonstrated by transient absorption (TA) spectroscopy. Furthermore, the mechanistic insights into photoreduction of CO_2 have been studied based on thermodynamical, electrochemical, and spectroscopic investigation, together with density functional theory (DFT) calculations.

2. Experimental

2.1. Sample preparation

Synthesis of $[Ru(dcbpy)(bpy)_2]Cl_2$ (Ru-H_2L) and bpet: the two ligands were synthesized according to previously published procedures [29,30]; synthetic details are provided in the Supporting Information (Figs. S1 and S2 online).

Synthesis of $[Ni^{II}(bpet)(H_2O)_2]\cdot(ClO_4)_2$: the Ni(II) complex was prepared by stirring 30 mL of methanolic solution containing $Ni(ClO_4)_2\cdot6H_2O$ (365.7 mg, 1.0 mmol) and bpet (276 mg, 1.0 mmol), and the mixture was stirred for 20 h at room temperature under N_2. The resultant blue precipitate was filtered and washed with CH_3OH. Then, the resulting Ni(II) complex was purified by recrystallizations from acetonitrile/H_2O gave light green crystals (478.1 mg, 65% yield, Figs. S3 and S4, Tables S1 and S2 online). Anal. Calcd. for $C_{14}H_{20}Cl_2N_2NiO_{10}S_2$: C 29.50, H 3.54, N 4.91, S 11.25, found: C 29.35, H 3.27, N 4.82. S 11.13. ESI-MS (CH_3CN): *m/z* 432.952 (calcd. for $[-2H_2O\text{-}ClO_4]^+$), *m/z* 167.00 (calcd. for $[-2H_2O\text{-}2ClO_4]^{2+}$, Fig. S5 online).

Synthesis of $[Zr_6(\mu_3\text{-}O)_4(\mu_3\text{-}OH)_4(bpdc)_{5.7}(Ru\text{-}L)_{0.3}]\cdot(OAc)_{0.6}$ (Ru-UiO-67): a mixture of $ZrCl_4$ (30.0 mg, 0.129 mmol), 4,4′-biphenyldi carboxylic acid (H_2bpdc) (26.6 mg, 0.110 mmol), Ru-H_2L (13.0 mg, 0.018 mmol), and glacial acetic acid (250 μL) were dispersed in *N, N*-dimethylformamide (DMF) (5 mL), sealed in a screw-capped glass vial and placed heated at 100 °C for 48 h with a heating speed of 3 °C min^{-1}. After cooling down to room temperature, the resulting solid was isolated by centrifugation and washed with DMF (3 × 15 mL) and methanol (3 × 15 mL) repeatedly. Yield: 45 mg (75%). The Ru-H_2L ligand content in Ru-UiO-67 was determined by inductively coupled plasma-mass spectrometry (ICP-MS) to be 8.7 wt%. Molar doping level (mol Ru-L/(mol bpdc + mol Ru-L)) was calculated from the ICP-MS result to be 5.0%.

Synthesis of $[Zr_6(\mu_3\text{-}O)_4(\mu_3\text{-}OH)_4(bpdc)_{5.7}(Ru\text{-}L)_{0.3}][Ni^{II}(bpet)(H_2O)_2]_x\cdot(OAc)_y$ (Ni1@Ru-UiO-67, $x = 0.00915$, $y = 0.6183$; Ni2@Ru-UiO-67, $x = 0.014$, $y = 0.628$ and Ni3@Ru-UiO-67, $x = 0.019$, $y = 0.638$): for the synthesis of Ni1@Ru-UiO-67, typically, 100 mg of Ru-UiO-67 was suspended in 20 mL of acetonitrile in a conical flask. Then 50 mg of bpet (0.18 mmol) was added with continuous stirring 48 h for the encapsulation of bpet under N_2. Subsequently the suspension was centrifuged and washed with acetonitrile three more times until the filtrate was colorless to remove the adsorbed bpet ligand on the outer surface of Ru-UiO-67. After suspending the washed wet solid in 20 mL of fresh acetone, 146 mg of $Ni(ClO_4)_2\cdot6H_2O$ (0.4 mmol) and 1 mL H_2O were added under continuous stirring. To promote the coordination between Ni(II) and bpet ligand, the suspension was stirred for 24 h under N_2. Then the suspension was centrifuged and washed with acetonitrile three times to remove the residual $Ni(ClO_4)_2$. The obtained solid was then dried in a 70 °C vacuum oven overnight to obtain Ni1@Ru-UiO-67. The Ni2@Ru-UiO-67 and Ni3@Ru-UiO-67 were prepared following the same procedure except changing the amounts of both bpet ligand and $Ni(ClO_4)_2\cdot6H_2O$ as listed in Table S3 (online). ICP-MS shows that the loadings of Ni(II) complex in Ni@Ru-UiO-67 composites were 0.15 wt% for Ni1@Ru-UiO-67, 0.23 wt% for Ni2@Ru-UiO-67 and 0.31 wt% for Ni3@Ru-UiO-67 with the elemental ratio of Ru:Ni = 32.8:1, 21.4:1 and 15.9:1. In addition, the color change of Ru-UiO-67 during the synthesis also indicate the successful encapsulation of Ni(II) complex and the achievement of a Ni@Ru-UiO-67 composites (Fig. S6 online). Noteworthy, to improve the loading capacity of Ru-UiO-67, the as-synthesized Ru-UiO-67 solid was dispersed in DMF and kept stirring overnight (50 mL of DMF per 1 g of product) to remove residual linker. Then, the same procedure was repeated twice using CH_3CN instead of DMF to exchange the DMF within the pores. The solid was finally dried under air at 100 °C.

2.2. Characterizations

Powder X-ray diffraction (PXRD) patterns of the samples were collected with a Rigaku Ultima IV diffractometer with Cu Kα radiation ($\lambda = 0.15406$ nm) operating. X-ray photoelectron spectroscopy (XPS) measurements were performed on an ESCALAB 250Xi instrument (Thermo Electron) with Al Karadiation. Fourier-transform infrared (FTIR) spectra were recorded on a Nicolet AVATAR FT-IR360 spectrophotometer. Inductively coupled plasma-mass spectrometry (ICP-MS) data were obtained with an Agilent 7700x ICP-MS. Thermogravimetric analyses were performed on a Q600 thermal analyzer. Solid-state UV–vis diffuse absorption spectra were recorded on a Cary-5000 UV–vis spectrometer within a wavelength range of 200–800 nm. Steady-state luminescence quenching spectra were obtained using a F-7000 FL spectrophotometer. Time-resolved photoluminescence spectra were recorded on an Edinburgh Instruments FLS 980 fluorimeter. Electrospray ionization mass spectra (ESI-MS) were obtained on a Agilent Technologies ESI-MS spectrometer. The Brunauer-Emmett-Teller (BET) surface areas of the catalysts were determined using N_2 adsorption–desorption isotherms measured on a Micromeritics Surface Area Analyzer (ASAP 2020) at 77 K. Scanning electron microscope (SEM) images were obtained on a high resolution S4800 scanning electron microscope operating at 30 kV. Transmission electron microscopy (TEM) images were recorded with a JEOL JEM-2100.

2.3. Photocatalytic CO_2 reduction

In a typical experiment, Ni@Ru-UiO-67 (20 mg) was suspended in a mixed solution of DMF (27 mL), deionized water (3 mL), 1,3-dimethyl-2-phenyl-2,3-dihydro-1*H*-benzoimidazole (BIH, 0.1 mol/L) and triethanolamine (TEOA) (0.5 mol/L), then the suspension was purged with CO_2 gas for 30 min while stirring. The sample was irradiated continuously with a 82 W light-emitting diode (LED) lamp ($\lambda = 450$ nm) at 288 K. After each reaction time, the evolved gaseous phase were determined by a Aulight GC-7920 gas chromatography (GC, N_2 as a carrier gas) using the TCD (a packed column with molecular sieves 5A (3.0 m × 3.0 mm, 60–80 mesh) at 373 K) to detect H_2 and using the FID (a column (TDX-1, 3.0 m × 0.30 mm) at 653 K) to detect CO, respectively. The total

amounts of evolved H_2 and CO were quantified by a basis of calibration curves prepared for various concentrations of H_2 and CO.

3. Results and discussion

As illustrated in Fig. 1, a series of photoactive MOF-based composites with simultaneously incorporated Ru-photosensitizer and Ni(II) molecular catalyst were synthesized via a "ship-in-a-bottle" synthetic strategy. The as-synthesized Ru-UiO-67 and Ni@Ru-UiO-67 composites were fully characterized. As shown in Fig. 2a, XRD patterns of the three catalysts and Ru-UiO-67 samples match well with the prototype UiO-67 peaks, clearly demonstrating that the crystallinity of the Ru-UiO-67 host is maintained upon encapsulation of the Ni(II) complex. BET surface area measurements at 77 K calculated from the N_2 adsorption/desorption isotherms show BET surface area of 2,135, 1,210, 1,150, 1,040, 890 m^2/g were observed, respectively, for UiO-67, Ru-UiO-67, Ni1@Ru-UiO-67, Ni2@Ru-UiO-67 and Ni3@Ru-UiO-67 (Fig. 2b). The decrease in the BET surface area of the Ru-UiO-67 compared with pristine UiO-67, which is owing to the introduction of Ru $(bpy)_2$ groups in Ru-UiO-67. On the other hand, the decreased N_2 sorption of the composites indicate that the Ni(II) complex was indeed located in the Ru-UiO-67. Among them, the Ni3@Ru-UiO-67 exhibits the lowest BET surface area, revealing the highest loading of Ni(II) complex, which is in good agreement with the ICP-MS analysis indicated above. Infrared spectra of Ni3@Ru-UiO-67, ligands and Ni(II) complex were comparable with that of undoped Ru-UiO-67 (Fig. S7 online). Considerable similarities were observed between Ru-UiO-67 and Ni3@Ru-UiO-67 with minor differences in band position and shape. However, an increased band between 2,950–2,920 cm^{-1} assigned to typical of S-CH_2- stretching vibrations in Ni3@Ru-UiO-67 was observed, due to the encapsulation of the Ni(II) complex. As shown in Fig. 2c, the additional broad absorption in the range of 370–650 nm in Ni@Ru-UiO-67 and Ru-UiO-67 is attributed to the Ru(d_π^6) → Ru(d_π^5)bpy(π^*) metal-to-ligand charge transfer (MLCT) of singlet character. The difference of absorption spectrum between Ru-UIO-67 and Ni@Ru-UIO-67 is attributed to $\pi \rightarrow \pi^*$ of bpet ligand and the low-energy absorption of the metal-to-ligand ($d_\pi \rightarrow \pi^*$) charge transfer transition for Ni (II) complex in Ru-UIO-67. On the other hand, further evidence for the successful encapsulation of Ni(II) complex into Ru-UiO-67 was afforded by photoluminescence emission spectroscopy. As shown in Fig. 2d, the photoluminescence (PL) emission spectroscopy of Ni@Ru-UiO-67 composites are descending compared with that of Ru-UiO-67, not only attribute to the weaker absorption but also due to the electron transfer from the photoexcited state of the $[Ru(dcbpy)(bpy)_2]^{2+}$ units to the encapsulated neighbouring Ni(II) complex [31]. This is further supported by time-resolved photoluminescence measurements. As shown in Fig. S8 (online), the Ru-UiO-67 exhibits a lifetime of 385 ns, while Ni1@Ru-UIO-67, Ni2@Ru-UIO-67 and Ni3@Ru-UIO-67 show lifetime 156, 127 and 109 ns, respectively. Lifetime decreases and enhanced quenching effect of Ni@Ru-MOFs indicated that the facile electron transfer from the excited Ru-MOFs to encapsulated Ni(II) complex due to their proximity. Furthermore, the PL of Ni3@Ru-UiO-67 is much weaker than that of others, indicating the PL of Ru-UiO-67 is quenched by more Ni(II) complex. The efficient PL quenching reflected that electron transfer process was remarkably enhanced through the unique one-cage-one-guest encapsulation pattern. These results indicate that Ni3@Ru-UiO-67 will possess superior photocatalytic activity compared with Ni1@Ru-UiO-67 and Ni2@Ru-UiO-67.

The SEM observation for Ni3@Ru-UiO-67 and Ru-UiO-67 shows that the loading of the Ni(II) complex does not affect the MOF morphology, and the MOF crystals remain intact in the composites (Fig. S9 online). The detailed nanostructure of the Ni3@Ru-UiO-67 was further investigated by TEM. As shown in Fig. 2e, the Ni3@Ru-UiO-67 shows an octahedral morphology, which is in good agreement with SEM observations. The elemental mapping analysis of Ni, S, Ru and Zr performed on an extended area of a solid sample of Ni3@Ru-UiO-67 revealed that the elements were uniformly distributed inside the Ru-UiO-67, further attesting to the Ni(II) complex that was homogeneously encapsulated in the pores of the Ru-UiO-67. In addition, thermogravimetric analysis (TGA) of the UiO-67, Ru-UiO-67 and Ni3@Ru-UiO-67 were conducted in an N_2 atmosphere (Fig. S10 online). Similar to the pristine Ru-UiO-67, the Ni1@Ru-UiO-67, Ni2@Ru-UiO-67 and Ni3@Ru-UiO-67 also

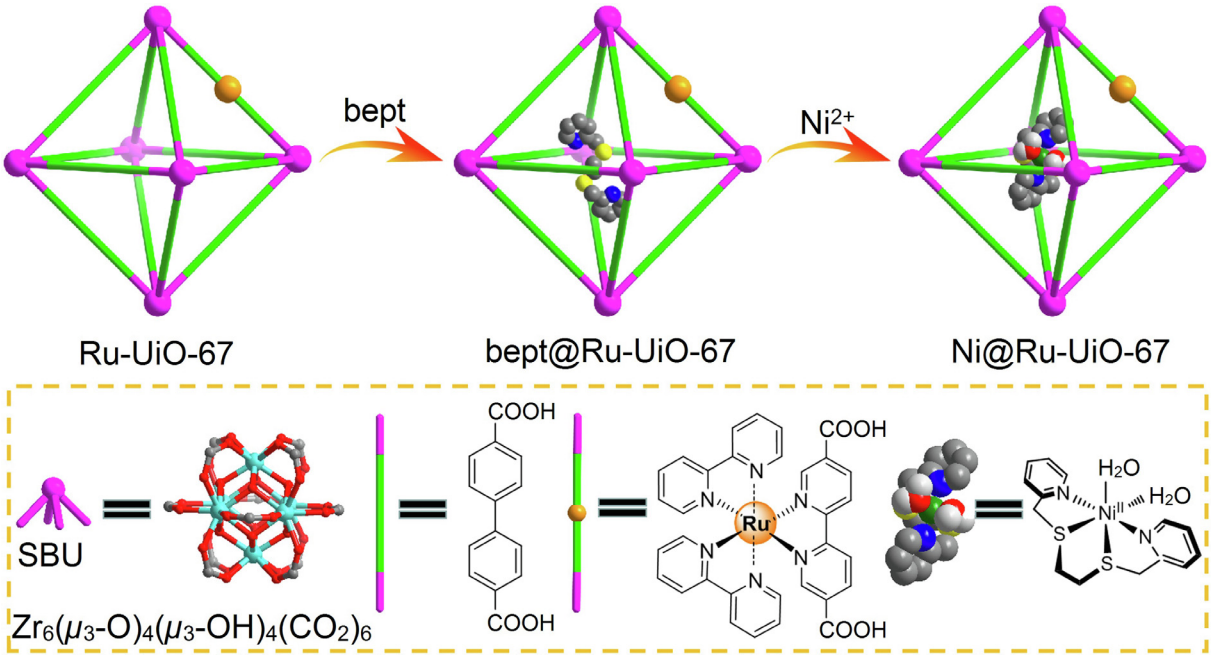

Fig. 1. (Color online) Schematic illustration for "Ship-in-a-Bottle" synthetic strategy to prepare Ni@Ru-UiO-67 composite.

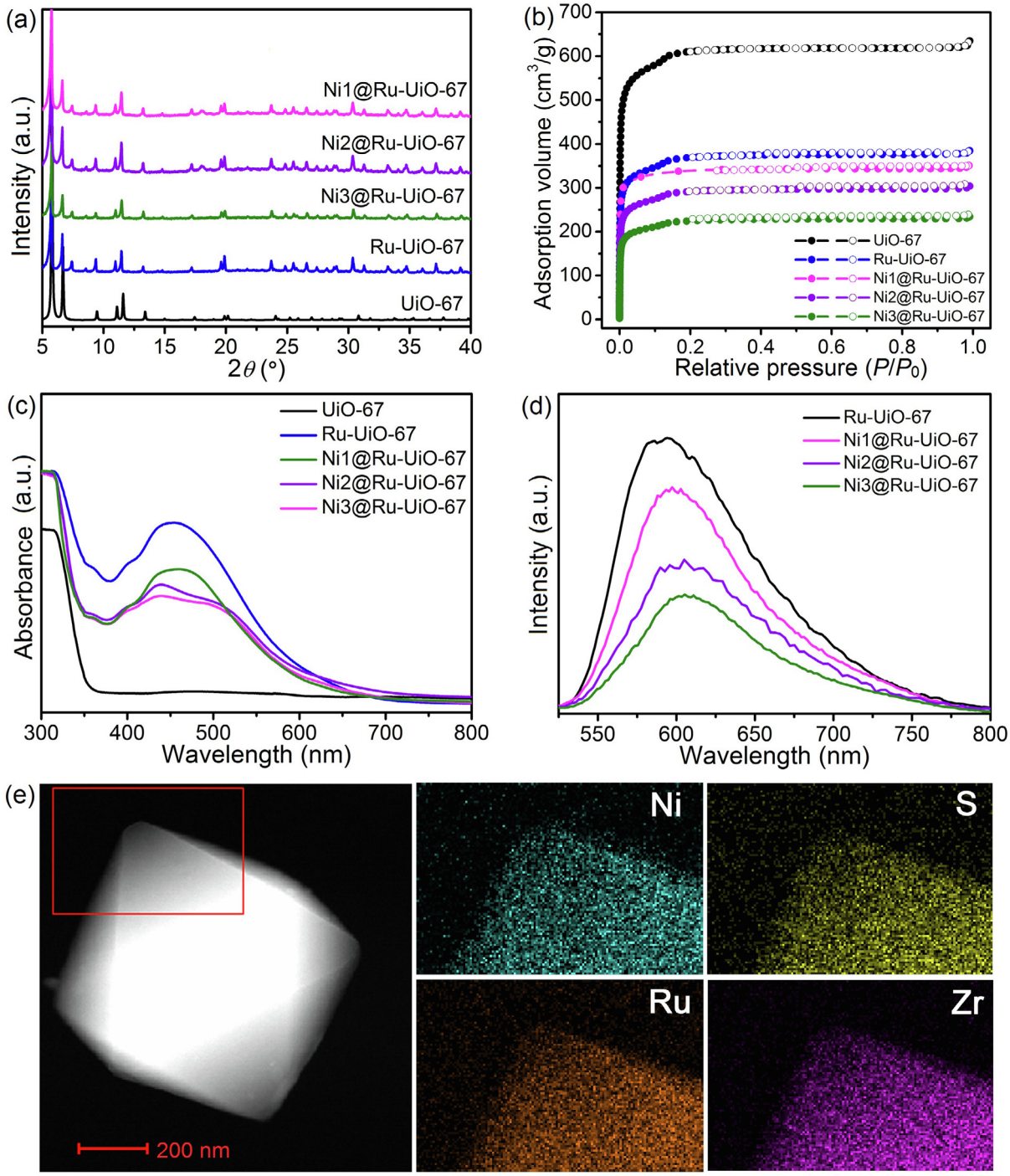

Fig. 2. (Color online) Characterization of Ru-UiO-67 and Ni@Ru-UiO-67 composites. PXRD patterns (a), N_2 adsorption/desorption isotherms (b), UV–vis spectra (c) and PL emission spectra (d) of UiO-67, Ru-UiO-67, Ni1@Ru-UiO-67, Ni2@Ru-UiO-67 and Ni3@Ru-UiO-67 (λ_{ex} = 446 nm, refer to its UV–vis spectrum). (e) TEM image of Ni3@Ru-UiO-67 and elemental mapping of the various elements (Ni, S, Ru, and Zr) contained in Ni3@Ru-UiO-67.

exhibited two decomposition steps at ~50 to 400 °C and >400 °C, respectively. The weight loss decreases between 50 and 250 °C, indicating that the Ni(II) complex replaces part of solvent molecules in the cage of the Ru-UiO-67.

XPS was carried out to analyze the chemical compositions and binding environments of the samples. Note that the electron binding energy not only depends on the element itself but also the chemical state in samples [32]. The XPS spectrum of Ni3@Ru-UiO-67 in Fig. 3a displays the signatures of C, O, N, S, Ru and Ni. As shown in Fig. 3b, the high-resolution S 2p XPS spectrum displays two broad peaks at 164.0 and 168.8 eV pertaining to S $2p_{1/2}$ and S $2p_{3/2}$, respectively [33]. The S 2p peaks were attributed to the bound nickel-thiol species [34]. A high-resolution XPS Ni 2p spectrum shows the peaks at 856.7 eV (Ni $2p_{3/2}$) and 873.8 eV (Ni $2p_{1/2}$) (Fig. 3c) [35], which corresponds to the peak position of Ni-S [36]. As shown in Fig. 3a and d, the peaks at 484.7 eV (Ru $3p_{3/2}$) and 462.6 eV (Ru $3p_{1/2}$) in both Ru-UiO-67 and Ni@Ru-UiO-67 are in agreement with the pattern of Ru^{2+}. All the above results demonstrate that Ni(II) complex was successfully encapsulated into the robust Ru-UiO-67.

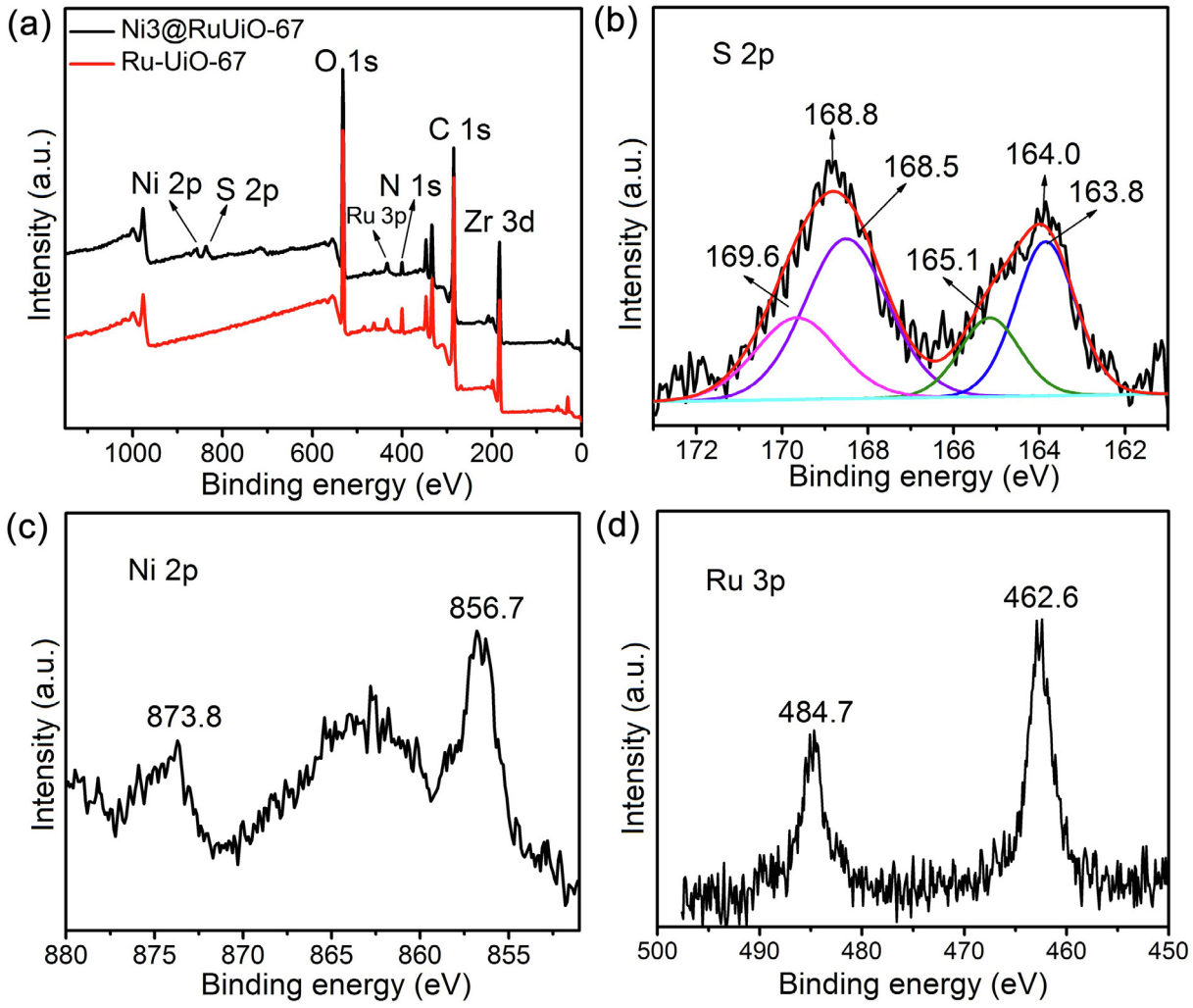

Fig. 3. (Color online) XPS experiments for Ni3@Ru-UiO-67. Survey scan XPS spectra in the binding energy range 0–1,100 eV of Ru-UiO-67 and Ni3@Ru-UiO-67 (a), high-resolution spectra of S 2p (b), Ni 2p (c) and Ru 3p (d) in Ni3@Ru-UiO-67.

The photocatalytic CO_2 reduction of Ni@Ru-UiO-67 composites were performed in a closed gas circulation and evacuation system. Each of the catalyst (20 mg) was independently suspended in a mixture of DMF (27 mL), deionized water (3 mL), BIH (0.1 mol/L), and TEOA (0.5 mol/L), which was deoxygenated by CO_2 and irradiated with a LED light (82 W). BIH as a sacrificial reductant can efficiently quench the excited state of photosensitizer, whereas TEOA mainly functions as a proton acceptor for $BIH^{+\bullet}$ [37]. As shown in Fig. 4a, the generation of CO increases almost linearly with irradiation time upon 10 h. Ni3@Ru-UiO-67 exhibits the CO evolution rate of 426.05 μmol/(g h) (85.21 μmol) with a catalytic turnover number (TON) of 510.0 (defined as $n(CO)/n(Ni(bpet)(H_2O)_2)$, which holds a high catalytic performance among reported MOF catalysts (Table S4 online) [38,39]. Notably, only a negligible amount of H_2 could be detected (Fig. S11 online), and no formate was detected by HPLC analysis and ^1H NMR spectroscopy (Figs. S12 and S13 online). The CO evolution rates of 55.25 μmol/(mg h) (yield: 11.05 μmol, TON: 136.7) and 196.80 μmol/(g h) (yield: 39.36 μmol, TON: 317.5) were obtained for Ni1@Ru-UiO-67 and Ni2@Ru-UiO-67, respectively. After 20 h irradiation, the TON of CO production of Ni3@Ru-UiO-67 was reached 581 with CO selectivity of >99% (calculated as TON (CO)/TON(CO + H_2)), indicating that Ni3@Ru-UiO-67 can photo-reduce CO_2 to CO selectively. Control experiments only with BIH or TEOA of Ni3@Ru-UiO-67 showed the TON for CO were 216.1 and 60.7, respectively (Fig. 4b), suggesting that TEOA is advantageous for reduction of CO_2. As previously reported [40], BIH can dramatically enhanced TON in the photocatalytic CO_2 reduction because of its high reductive ability, fast deprotonation of the oxidized BIH species ($BIH^{+\bullet}$), and two-electron donating ability. On the other hand, to demonstrate the unique advantage of the Ni3@Ru-UiO-67 composite, we compared the photocatalytic activities of Ni3@Ru-UiO-67 to that of homogeneous $[Ni^{II}(bpet)(H_2O)_2]$/Ru-H_2L (the Ni(II) complex with the same Ni loading as that in Ni3@Ru-UiO-67) as control. As shown in Fig. 4a, the activity of $[Ni^{II}(bpet)(H_2O)_2]$ is similar with that of Ni3@Ru-UIO-67 at the first 5 h. With increasing the reaction time, the activities of $[Ni^{II}(bpet)(H_2O)_2]$ decrease because of the self-aggregation and oxidative self-degradation, while the activities of Ni3@Ru-UIO-67 can be stabilized up to 10 h. The results demonstrate that encapsulating molecular catalyst into photoactive MOF is a promising approach to design efficient, stable and recyclable photocatalysts. It should be noted, compared with the reported photocatalytic activity of $[Ni^{II}(bpet)(H_2O)_2]$ [18], the TON value of 280 of $[Ni^{II}(bpet)(H_2O)_2]$ in this work is higher than the reported experimental value (ca.180) at the first 5 h, but the stability in this work is lower. The reason may be attributed to the higher power light source in this work (a 82 W LED for this work and a 6 W LED for reported experiment). In addition, the

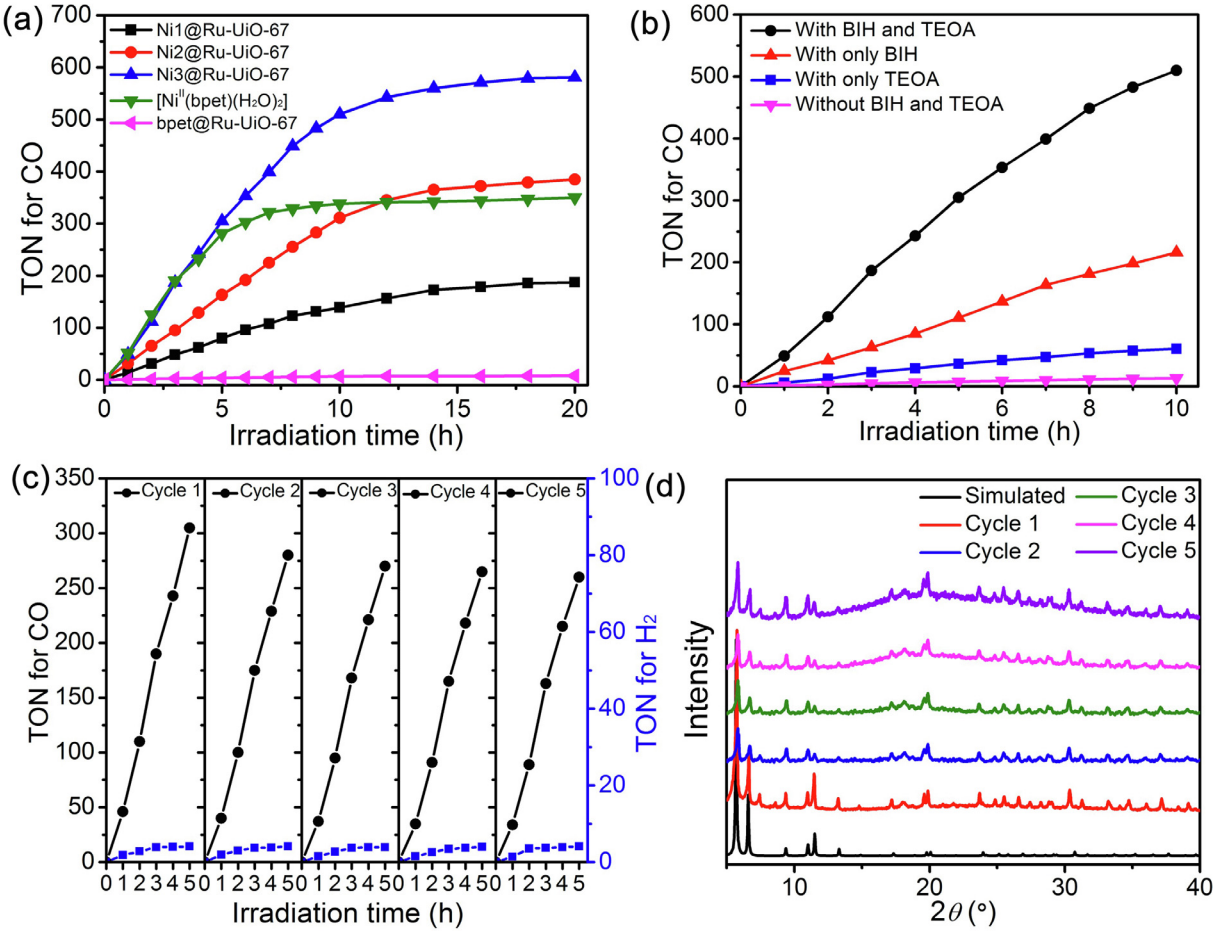

Fig. 4. (Color online) Photocatalytic CO_2 reduction performance. (a) Time profiles of CO evolution catalyzed by different catalysts under irradiation of a 450 nm LED light. (b) Profound influence on photocatalytic CO_2 reduction by BIH and TEOA. (c) Recyclability of Ni3@Ru-UiO-67 in five consecutive experiments. (d) Powder XRD patterns for Ni3@Ru-UiO-67 before and after every run of reaction.

different experimental conditions, such as, photosensitizer, solvents and concentration, may also be factors that affect the activity and stability of the [Ni^{II}(bpet)(H$_2$O)$_2$].

Confirmation of the carbon source is essential for photocatalytic CO_2 reduction in heterogeneous systems. Isotopic labeling experiment was performed with $^{13}CO_2$, and the gaseous product was detected by GC-mass spectroscopy (GC–MS) to investigate the carbon source of the produced CO. After 6 h of visible-light irradiation, GC–MS analysis showed clearly the signals of ^{13}CO (m/z 29). In contrast, the signal was absent in the GC–MS spectra when $^{12}CO_2$ was used as the reactant (Fig. S14 online), unambiguously confirming that CO was generated from CO_2 photoreduction.

In order to evaluate the stability of Ni@Ru-UiO-67 composite, the catalyst durability tests were carried out under the optimized conditions taking into account the relatively high CO evolution rate. The recycling tests were explored by collecting catalyst after each 5 h illumination via centrifugation and dispersal in a fresh catalysis solution. Fig. 4c shows TON of CO and H_2 for Ni3@Ru-UiO-67 as a function of time in consecutive five reaction cycles. Although the CO evolution dependence on time deviates from linearity gradually after 10 h, the initial rate in every run can be evaluated from the slope of straight line portion at the first 5 h. The highest rate of 10.19 μmol/h appears in the first run, and there is only a slight decrease in the fifth run (Fig. S15 online). PXRD analyses of Ni3@Ru-UiO-67 after photocatalytic reaction showed no significant change in the diffraction patterns, suggesting its structural stability (Fig. 4d). Furthermore, after the fifth run, the concentration of Ni in the supernatant solution before and after catalysis were measured by ICP-MS to examine the possibility of Ni leaching, indicated that less than 0.5% of Ni was leached into the solution during catalysis process. The high activity and good durability of Ni3@Ru-UiO-67 demonstrate the great potential in photocatalytic CO_2 reduction.

In order to uncover the photocatalytic mechanism of Ni@Ru-UiO-67 system, the electrochemical properties of Ni(II) complex were investigated by cyclic voltammetry (CV) in a solution of DMF/H_2O (9:1, v:v) under N_2 atmosphere. As described in Fig. 5a, two irreversible reductive waves are attributable to step-by-step reduction and changes of octahedral Ni^{II} to tetrahedral Ni^0 complexes. The first wave of Ni(II) complex at −0.60 V (vs. NHE) can be assigned to be the reduction of the Ni center from Ni^{II} to Ni^{I} and the second cathodic wave at −0.79 V (vs. NHE) was corresponded to a metal-centered Ni^{I}/Ni^0 redox process. Moreover, the oxidative peak observed at around 0.5 V is likely due to the ligand-centred oxidation of tetrahedral Ni^0 complexes [41]. This result reflects that the excellent activity of Ni@Ru-UiO-67 composite is correlated with the reduction of the Ni(II) complex.

To confirm the thermodynamic feasibility of photoinduced electron transfer (PET) and the driving force for the reduction of CO_2, the free energy change (ΔG^0) was introduced which can be used to estimate a PET process from Ru-H_2L to Ni(II) complex. The ΔG^0 is calculated by the Rehm-Weller equation (Eq. (1)) [42]:

$$\Delta G^0 = E_{ox} - E_{red} - E_{00} - C, \quad (1)$$

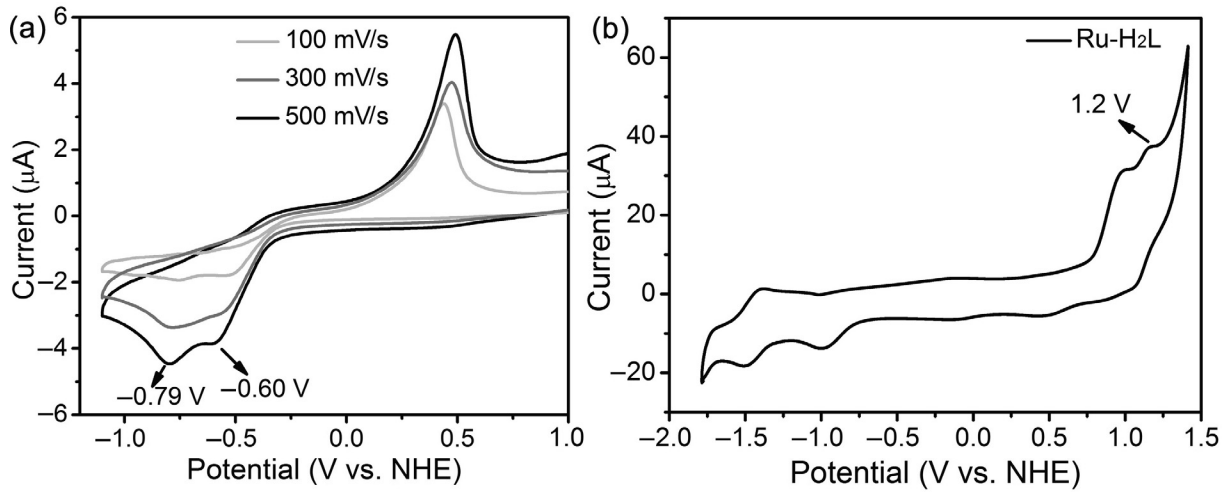

Fig. 5. Electrochemical characterization of samples. CVs of Ni(II) complex (a) and Ru-H_2L (b) in a DMF/H_2O (9:1, v:v) solution containing 0.10 mol/L of $TBAPF_6$ (TBA = tetra-*n*-butylammonium) under N_2.

$$C = \frac{e^2}{\varepsilon d}, \tag{2}$$

where, E_{ox} is the oxidative potential of the species donating an electron (Ru-H_2L), E_{red} is the reductive potential of the species accepting an electron (Ni(II) complex), E_{00} is the energy difference between the ground and excited states of the photosensitizer and C is the sum of the solvation effect that accounts for the change in coulombic interactions due to the charge shift in solution. As the dielectric constants of the polar solvents DMF are quite high, the term C could be negligible (Eq. (2)) [43]. As shown in Fig. 5, CVs of Ni(II) complex and Ru-H_2L show that the first oxidation E_{ox} of Ru-H_2L is 1.20 V (vs. NHE) and the first reduction E_{red} of Ni(II) complex is −0.60 V (vs. NHE). The E_{00} value of 2.10 V can be calculated from the luminescence emission peak at 590 nm of Ru-H_2L at room temperature (Fig. S8a online). Fitting of the above data to Eq. (1), a negative ΔG^0 of −0.30 V was obtained, suggesting the PET progress from Ru-H_2L to Ni(II) is thermodynamically favourable.

In order to investigate the excited state (ES) and electron transfer (ET) dynamics in Ni@Ru-UiO-67 composite, we also carried out the optical transient absorption (TA) measurements. Fig. 6a shows the ultrafast TA spectra of Ru-UiO-67 and Ni3@Ru-UiO-67 at the selected delay times after the excitation at 450 nm. The TA spectra of Ru-UiO-67 was used as a control to illustrate the intrinsic ES dynamics of Ru-moiety in MOF framework without Ni(II) molecular catalyst. The spectra of Ru-UiO-67 exhibits two instantaneously formed spectral features, a negative band centered at ~530 nm and a broad photoinduced positive absorption features between 620 and 770 nm, which can be attributed to the ground state bleach (GSB) and excited state absorption (ESA) of Ru-moiety, respectively. Such transient absorption profile of Ru-UiO-67 is similar with those of reported in literatures containing Ru-moiety complex [44]. Similar to the spectra of Ru-UiO-67, the TA spectra of Ni3@Ru-UiO-67 also show two main spectral features, a GSB band centred at ~520 nm and a broad ESA band in 570–770 nm region. The whole spectra of Ni3@Ru-UiO-67 shift to shorter wavelengths with respect to that of Ru-UiO-67 because of the formation of a ET state between Ru-moiety and Ni(II) complex, which is consistent with their steady-state spectrum [45]. Furthermore, the amplitude of GSB at 520 nm increases within 7 ns, distinctly different to that of Ru-UiO-67. These spectroscopic features indicate that the excited state of Ni3@Ru-UiO-67 turned into the reduced state due to electron transfer processes, but rather than relaxing to ground state as in the neat Ru-UiO-67. As illustrated in Fig. 6b,

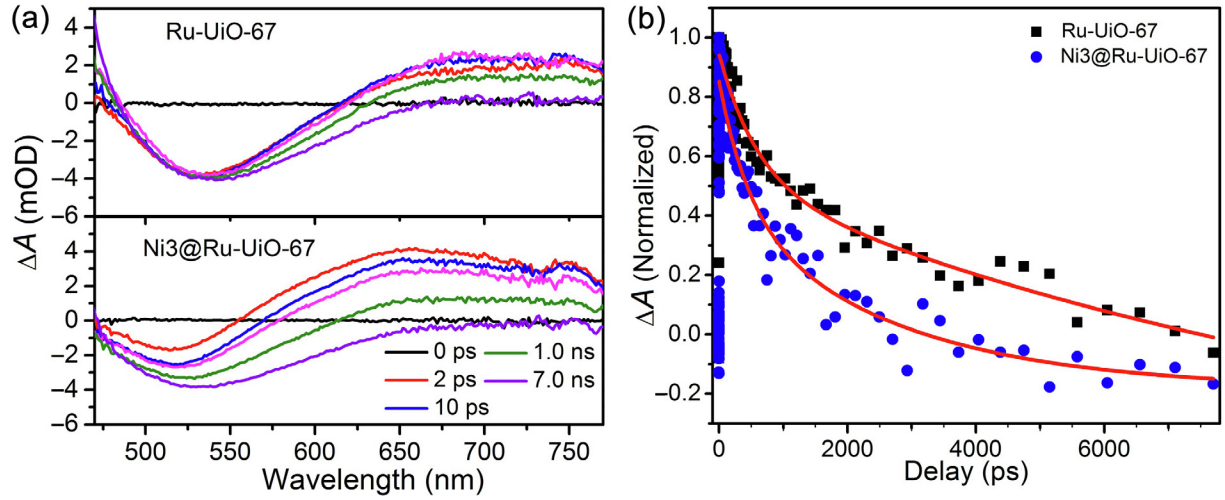

Fig. 6. (Color online) Spectroscopic evidence for effective charge separation process. (a) Femtosecond TA spectra of Ru-UiO-67 and Ni3@Ru-UiO-67. (b) The comparisons of ES decay kinetics between Ru-UiO-67 and Ni3@Ru-UiO-67.

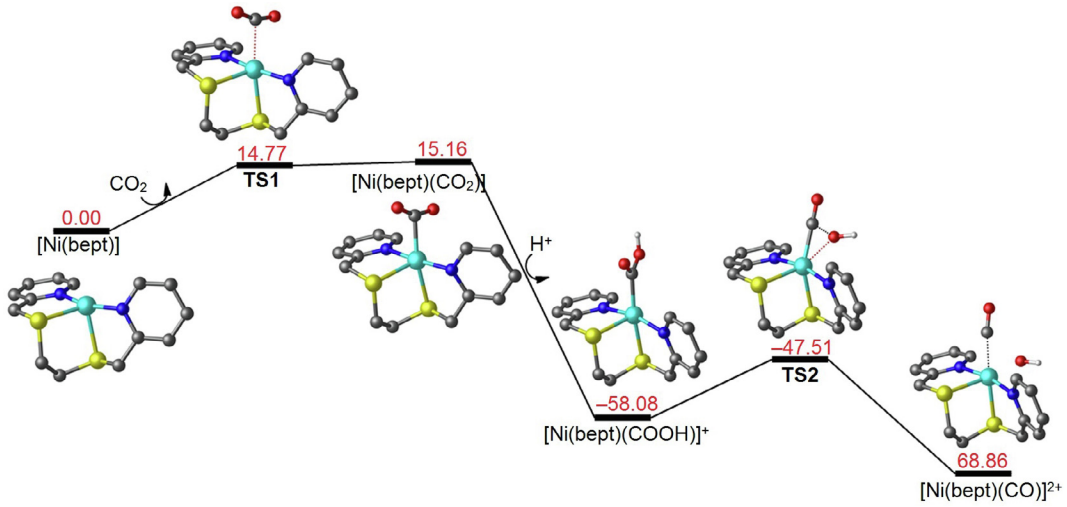

Fig. 7. (Color online) Potential energy surface showing reaction pathway for the photocatalytic CO_2 reduction at the cam-B3LYP/6–311 + G(d,p) level in DMF.

the ESA kinetics in Ni3@Ru-UiO-67 decays faster than that in Ru-UiO-67, further supporting the ET process from excited Ru-H_2L to Ni(II) complex in Ni3@Ru-UiO-67.

To further investigate the catalytic mechanism of Ni(bpet)$(H_2O)_2$, we carried out the DFT calculations (see the Supporting Information online) [46], which can probe the active site of Ni(II) complex and the adsorption energy and charge difference density of CO_2 adsorption structure. The relaxed structure feature pseudo-C_2 symmetry with two geometrically equivalent coordinated H_2O molecules. The optimized configuration reflects that the H_2O was easy removed, and the desorption free energy was $\Delta G = -0.90$ kcal/mol. Therefore, one Lewis acid catalytic site was exposed on the unsaturated Ni(II) ions after H_2O were removed under visible light irradiation The unsaturated Ni(II) ions can further adsorb one CO_2 molecule. As shown in Fig. 7, for DFT calculations, two possible activation energy barriers were taken into consideration, one is the CO_2-binding step to give the Ni-CO_2 intermediate (**TS1**, $\Delta G_1^{\ddagger}$) and the other is the CO-cleavage step to form Ni-CO species (**TS2**, $\Delta G_2^{\ddagger}$). The CO_2 molecule binds to the reduced Ni^0 through the carbon atom forming Ni–CO_2 species (transition state **TS1**, Fig. S16a online), and the total barrier calculated for **TS1** is 14.77 kcal mol^{-1}. Meanwhile, the CO_2 molecule of **TS1** turns to distorted configuration with the angle of O-C-O (158.6°) and C-Ni bond length (2.24 Å). Then, the Ni-CO_2 species is protonated to form Ni-COOH intermediates, and, the C-OH bond in Ni-COOH species is cleaved at Ni center to generate Ni-CO species (transition state **TS2**, Fig. S16b online) and OH^- with the total energy barrier 10.57 kcal/mol for **TS2**. Simultaneously, the cleaved OH^- further reacts with a proton to form water. After the release of CO, Ni(bpet)$(H_2O)_2$ is regenerated and the catalytic cycle restarts. On the other hand, natural charge analysis indicates that CO_2 molecule behaves −0.822e for O, 0.711e for C and −0.777e charge for another O, while Ni ion features 0.100e charge. Obviously, under the light irradiation, CO_2 gets electrons from Ni ions, suggesting that the CO_2 molecule can be activated effectively by the Ni ion. Thus, the unsaturated site of Ni ion serves as active site in CO_2 photocatalytic reduction.

Based on the above experimental results and theoretical calculations, we propose the following reaction mechanism for photocatalytic CO_2 reduction in Ni@Ru-UiO-67 system. As shown in Fig. 8, under the visible-light irradiation, the ligand [Ru(dcbpy)$(bpy)_2]^{2+}$ will be excited forming the triplet MLCT excited state, ^{3}[Ru(dcbpy)$(bpy)_2]^{2+*}$, which is subjected to a reductive quenching by one electron from BIH (indicated by Stern-Volmer experiment, Fig. S17 online), then afforded [Ru(dcbpy)$(bpy)_2]^+$ and oxidized BIH ($BIH^{+\bullet}$). However, $BIH^{+\bullet}$ is easily deprotonated,

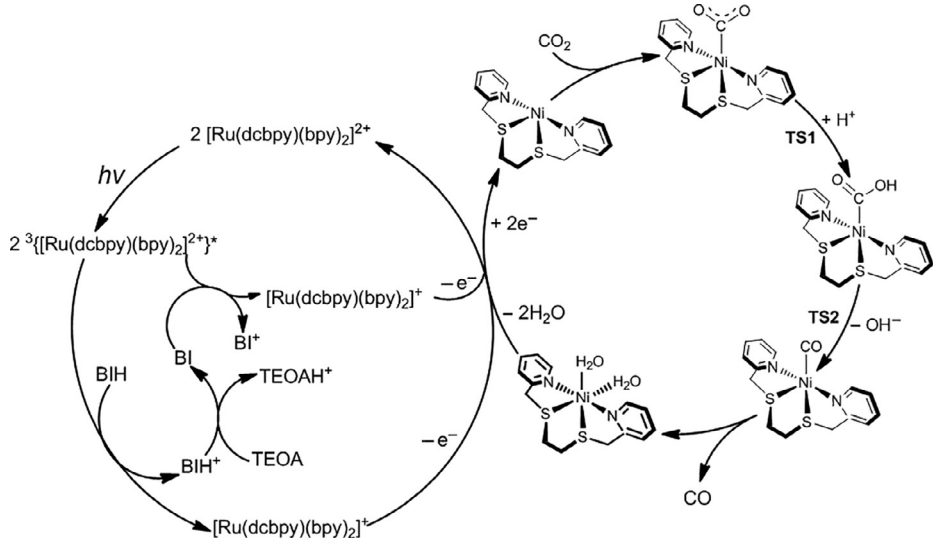

Fig. 8. Proposed mechanism for the photocatalytic reduction of CO_2 to CO in the Ni@Ru-UiO-67/BIH/TEOA system.

the deprotonated $BI^{\bullet}$ can supply one more electron to reduce another $^{3}[Ru(dcbpy)(bpy)_2]^{2+*}$ producing 2 equiv. of $[Ru(dcbpy)(bpy)_2]^{+}$ in the overall photoinduced process. Then Ni(II) complex was reduced by two $[Ru(dcbpy)(bpy)_2]^{+}$ to afford a $[Ni^{0}(bpet)]$ intermediate and two $[Ru(dcbpy)(bpy)_2]^{2+}$ with a two-electrons process. Finally, CO_2 binds to the reduced Ni^0 through the carbon atom forming a Ni-CO_2 adduct, after which protonation gives CO and regenerates the catalyst, completing the catalytic cycle. On the other hand, the formation of H_2 could result from the reduction of the existing protons in the reaction system by the light-induced electrons. Noteworthy, in the reduction process TEOA works as a base for $BIH^{+\bullet}$, which should suppress back electron transfer from [Ni(bpet)] to $BIH^{+\bullet}$ as one of the obstruction processes of the photocatalytic reduction (Fig. S18 online) [47].

4. Conclusions

In summary, we have synthesized a series of photoactive MOF-based composites with simultaneously incorporated Ru-photosensitizer and Ni(II) molecular catalyst via a "ship-in-a-bottle" synthetic strategy. The Ni@Ru-UiO-67 composites exhibit highly active, selective and robust, for photocatalytic CO_2 to CO conversion, with an optimal TON of 581. Moreover, the excellent heterogeneous catalyst exhibits outstanding stability after five repetitive reactions. The combination of advanced ultrafast absorption spectroscopy and theoretical calculations demonstrate the photoelectrons produced by Ru-L directly transfer to the Ni(II) catalyst affording Ni^0 species for reducing CO_2 to CO. The efficient charge transfer between Ru-UiO-67 and Ni(II) complex is responsible for its excellent activity. This work not only afford a rational strategy for synthesizing high-performance heterogeneous photocatalyst through encapsulating homogeneous molecular catalysts in photoactive MOF, but also provides a unique perspective for understanding the photocatalytic mechanism.

Conflict of interest

The authors declare that they have no conflict of interest.

Acknowledgments

This work was supported by the National Natural Science Foundation of China (21871224, 21673184, 21431005, and 21390391), the Fok Ying Tong Education Foundation (151013), and the Fundamental Research Funds for the Central Universities (20720180032).

Author contributions

Zhi-Hao Yan and Xiang-Jian Kong conceived and designed the research; Zhi-Hao Yan performed the research; Bo Ma and Gui-Lin Zhuang preformed the DFT calculations; Shu-Rong Li, Rong Chen and Ming-Hao Du participated in part of experiments; Junxue Liu and Shengye Jin measured TA spectra. Zhi-Hao Yan, Xiang-Jian Kong, La-Sheng Long and Lan-Sun Zheng analyzed data. Zhi-Hao Yan, Xiang-Jian Kong, and Shengye Jin wrote the manuscript with contributions from all authors. All authors discussed the results and commented on the manuscript.

Appendix A. Supplementary data

Supplementary data to this article can be found online at https://doi.org/10.1016/j.scib.2019.05.014.

References

[1] Tu W, Zhou Y, Zou Z. Photocatalytic conversion of CO_2 into renewable hydrocarbon fuels: state-of-the-art accomplishment, challenges, and prospects. Adv Mater 2014;26:4607–26.
[2] Dhakshinamoorthy A, Navalon S, Corma A, et al. Photocatalytic CO_2 reduction by TiO_2 and related titanium containing solids. Energy Environ Sci 2012;5:9217–33.
[3] Ozin DA. Throwing new light on the reduction of CO_2. Adv Mater 2015;27:1957–63.
[4] Kuriki R, Ichibha T, Hongo K, et al. Narrow-gap oxyfluoride photocatalyst for visible-light hydrogen evolution and carbon dioxide reduction. J Am Chem Soc 2018;140:6648–55.
[5] Zhao Y, Liu Z. Recent advances in photocatalytic CO_2 reduction using earth-abundant metal complexes-derived photocatalysts. Chin J Chem 2018;36:455–60.
[6] Wang Y, Huang NY, Shen JQ, et al. Hydroxide ligands cooperate with catalytic centers in metal-organic frameworks for efficient photocatalytic CO_2 reduction. J Am Chem Soc 2018;140:38–41.
[7] Xu HQ, Hu J, Wang D, et al. Visible-light photoreduction of CO_2 in a metal-organic framework: boosting electron-hole separation via electron trap states. J Am Chem Soc 2015;137:13440–3.
[8] Kajiwara T, Fujii M, Tsujimoto M, et al. Photochemical reduction of low concentrations of CO_2 in a porous coordination polymer with a ruthenium(II)-CO complex. Angew Chem Int Ed 2016;55:2697–700.
[9] Fu Y, Sun D, Chen Y, et al. An amine-functionalized titanium metal-organic framework photocatalyst with visible-light-induced activity for CO_2 reduction. Angew Chem Int Ed 2012;51:3364–7.
[10] Fujiwara H, Hosokawa H, Murakoshi K, et al. Effect of surface structures on photocatalytic CO_2 reduction using quantized CdS nanocrystallites. J Phys Chem B 1997;101:8270–8.
[11] Yan SC, Ouyang SX, Gao J, et al. A room-temperature reactive-template route to mesoporous $ZnGa_2O_4$ with improved photocatalytic activity in reduction of CO2. Angew Chem Int Ed 2010;49:6400–4.
[12] Liu Q, Zhou Y, Kou J, et al. High-yield synthesis of ultralong and ultrathin Zn_2GeO_4 nanoribbons toward improved photocatalytic reduction of CO_2 into renewable hydrocarbon fuel. J Am Chem Soc 2010;132:14385–7.
[13] Habisreutinger SN, Schmidt-Mende L, Stolarczyk JK. Photocatalytic reduction of CO_2 on TiO_2 and other semiconductors. Angew Chem Int Ed 2013;52:7372–408.
[14] Takeda H, Ohashi K, Sekine A, et al. Photocatalytic CO_2 reduction using Cu(I) photosensitizers with a Fe(II) catalyst. J Am Chem Soc 2016;138:4354–7.
[15] Guo Z, Cheng S, Cometto C, et al. Highly efficient and selective photocatalytic CO_2 reduction by iron and cobalt quaterpyridine complexes. J Am Chem Soc 2016;138:9413–6.
[16] Ouyang T, Huang HH, Wang JW, et al. A dinuclear cobalt cryptate as a homogeneous photocatalyst for highly selective and efficient visible-light driven CO_2 reduction to CO in CH_3CN/H_2O solution. Angew Chem Int Ed 2017;56:738–43.
[17] Chan SLF, Lam TL, Yang C, et al. A robust and efficient cobalt molecular catalyst for CO_2 reduction. Chem Commun 2015;51:7799–801.
[18] Hong D, Tsukakoshi Y, Kotani H, et al. Visible-light-driven photocatalytic CO_2 reduction by a Ni(II) complex bearing a bioinspired tetradentate ligand for selective CO production. J Am Chem Soc 2017;139:6538–41.
[19] Niu K, Xu Y, Wang H, et al. A spongy nickel-organic CO_2 reduction photocatalyst for nearly 100% selective CO production. Sci Adv 2017;3:e1700921.
[20] Cheung PL, Machan CW, Malkhasian AYS, et al. Photocatalytic reduction of carbon dioxide to CO and HCO_2H Using *fac*-Mn(CN)(bpy)$(CO)_3$. Inorg Chem 2016;55:3192–8.
[21] Takeda H, Koizumi H, Okamoto K, et al. Photocatalytic CO_2 reduction using a Mn complex as a catalyst. Chem Commun 2014;50:1491–3.
[22] Wang W, Wang S, Ma X, et al. Recent advances in catalytic hydrogenation of carbon dioxide. Chem Soc Rev 2011;40:3703–27.
[23] Chen L, Luque R, Li Y. Controllable design of tunable nanostructures inside metal-organic frameworks. Chem Soc Rev 2017;46:4614–30.
[24] Wu CD, Zhao M. Incorporation of molecular catalysts in metal-organic frameworks for highly efficient heterogeneous catalysis. Adv Mater 2017;1605446.
[25] Zhang ZM, Zhang T, Wang C, et al. Photosensitizing metal-organic framework enabling visible-light-driven proton reduction by a Wells-Dawson-type polyoxometalate. J Am Chem Soc 2015;137:3197–200.
[26] Kong XJ, Lin Z, Zhang ZM, et al. Hierarchical integration of photosensitizing metal-organic frameworks and nickel-containing polyoxometalates for efficient visible-light-driven hydrogen evolution. Angew Chem Int Ed 2016;55:6411–6.
[27] Trickett CA, Helal A, Al-Maythalony BA, et al. The chemistry of metal-organic frameworks for CO_2 capture, regeneration and conversion. Nat Rev Mater 2017;2:17045.
[28] Zhang S, Li L, Zhao S, et al. Hierarchical metal-organic framework nanoflowers for effective CO_2 transformation driven by visible light. J Mater Chem A 2015;3:15764–8.
[29] Adhikary B, Liu S, Lucas CR. Comparative studies of mononuclear nickel(II) complexes with N_2S_x (x= 2–4) Ligands. Inorg Chem 1993;32:5957.
[30] Xie PH, Hou YJ, Zhang BW, et al. Spectroscopic and electrochemical properties of ruthenium(II) polypyridyl complexes. J Chem Soc Dalton Trans 1999:4217–21.

[31] Yan ZH, Du MH, Liu J, et al. Photo-generated dinuclear {Eu(II)}$_2$ active sites for selective CO_2 reduction in a photosensitizing metal-organic framework. Nat Commun 2018;9:3353.
[32] An B, Zhang J, Cheng K, et al. Confinement of ultrasmall Cu/ZnO_x nanoparticles in metal-organic frameworks for selective methanol synthesis from catalytic hydrogenation of CO_2. J Am Chem Soc 2017;139:3834–40.
[33] Zhang HL, Evans SD, Henderson JR, et al. Spectroscopic characterization of gold nanoparticles passivated by mercaptopyridine and mercaptopyrimidine derivatives. J Phys Chem B 2003;107:6087–95.
[34] Wang C, Shang J, Lan Y, et al. Metal-organic polyhedra cages immobilized on a plasmonic substrate for sensitive detection of trace explosives. Adv Funct Mater 2015;25:6009–17.
[35] Biesinger MC, Payne BP, Grosvenor AP, et al. Resolving surface chemical states in XPS analysis of first row transition metals, oxides and hydroxides: Cr, Mn, Fe, Co and Ni. Appl Surface Sci 2011;257:2717–30.
[36] Nesbitt HW, Legrand D, Bancroft GM. Interpretation of Ni 2p XPS spectra of Ni conductors and Ni insulators. Phys Chem Miner 2000;27:357–66.
[37] Tamaki Y, Ishitani O. Supramolecular photocatalysts for the reduction of CO_2. ACS Catal 2017;7:3394–409.
[38] Chen EX, Qiu M, Zhang YF, et al. Acid and base resistant zirconium polyphenolate-metalloporphyrin scaffolds for efficient CO_2 photoreduction. Adv Mater 2018;30:1704388.
[39] Zhang H, Wei J, Dong J, et al. Efficient visible-light-driven carbon dioxide reduction by a single-atom implanted metal-organic framework. Angew Chem Int Ed 2016;55:14310–4.
[40] Tamaki Y, Koike K, Morimoto T, et al. Substantial improvement in the efficiency and durability of a photocatalyst for carbon dioxide reduction using a benzoimidazole derivative as an electron donor. J Catal 2013;304:22–8.
[41] Grapperhaus CA, Mullins CS, Kozlowski PM, et al. Synthesis and oxygenation of a nickel(II) and zinc(II) dithiolate: an experimental and theoretical comparison. Inorg Chem 2004;43:2859–66.
[42] Wang F, Wang WG, Wang HY, et al. Artificial photosynthetic systems based on [FeFe]-hydrogenase mimics: the road to high efficiency for light-driven hydrogen evolution. ACS Catal 2012;2:407–16.
[43] Liao WM, Zhang JH, Wang Z, et al. Post-synthetic exchange (PSE) of UiO-67 frameworks by Ru/Rh half-sandwich units for visible-light-driven H_2 evolution and CO_2 reduction. J Mater Chem A 2018;6:11337–45.
[44] Yang S, Pattengale B, Lee S, et al. Real-time visualization of active species in a single-site metal-organic framework photocatalyst. ACS Energy Lett 2018;3:532–9.
[45] Pattengale B, Ludwig J, Huang J. Atomic insight into the W-doping effect on carrier dynamics and photoelectrochemical properties of $BiVO_4$ photoanodes. J Phys Chem C 2016;120:1421–7.
[46] Anisimo VI, Aryasetiawan F, Lichtenstein IA. First-principles calculations of the electronic structure and spectra of strongly correlated systems: the LDA+ U method. J Phys Condens Matter 1997;9:767–808.
[47] Nakajima T, Tamaki Y, Ueno K, et al. Photocatalytic Reduction of Low Concentration of CO_2. J Am Chem Soc 2016;138:13818–21382.

Zhi-Hao Yan is currently a Ph.D. candidate at the Department of Chemistry, Xiamen University. He received his M.S. degree at Qingdao University of Science and Technology in 2015. His research mainly focuses on the synthesis and photocatalytic property of MOFs.

Shengye Jin received his B.S. degree in Chemical Engineering from Dalian University of Technology in 2001, M.S. degree in Chemistry from Dalian Institute of Chemical Physics (DICP)-CAS in 2004, and Ph.D. degree in Physical Chemistry from Emory University (USA) in 2010. He did postdoctoral research at Argonne National Laboratory and Northwestern University from 2010 to 2013, where he worked on photochemical dynamics for solar energy conversion. Dr. Jin then joined the State Key Laboratory of Molecular Reaction Dynamics of DICP-CAS as a principle investigator in 2013.

Xiang-Jian Kong received his B.S. degree in Chemistry from Liaocheng University in 2003, and his Ph.D. degree in Chemistry from Xiamen University in 2009. He is now a professor in the Department of Chemistry at Xiamen University. He was a visiting scholar at The University of Arizona (2007–2008) and The University of Chicago (2014–2015). His research is focused on the synthetic and materials chemistry of cluster compounds containing lanthanide and lanthanide-transition metal elements.